EDGE ARTICLE

Check for updates

Tuning molecular aggregation to achieve highly bright AIE dots for NIR-II fluorescence imaging and NIR-I photoacoustic imaging†

Yanzi Xu,[a] Chunbin Li,[b] Ruohan Xu,[a] Ning Zhang,[a] Zhi Wang,[a] Xunan Jing,[a] Zhiwei Yang,[a] Dongfeng Dang, *[a] Pengfei Zhang ⓘ *[b] and Lingjie Meng ⓘ *[ac]

Currently, bright aggregation-induced emission luminogens (AIEgens) with high photoluminescence quantum yields (PLQYs) in the NIR-II region are still limited, and thus an efficient strategy to enhance NIR-II fluorescence performance through tuning molecular aggregation is proposed here. The synthesized donor–acceptor tailored AIEgen (DTPA-TBZ) not only exhibits an excellent absorptivity in the NIR-I region, but also good fluorescence signals in the NIR-II region with an emission extending to 1200 nm. Benefiting from such improved intramolecular restriction and aggregation, a significant absolute PLQY value of 8.98% was obtained in solid DTPA-TBZ. Encouragingly, the resulting AIE dots also exhibit a high relative PLQY of up to 11.1% with IR 26 as the reference (PLQY = 0.5%). Finally, the AIE dots were applied in high performance NIR-II fluorescence imaging and NIR-I photoacoustic (PA) imaging: visualization of abdominal vessels, hind limb vasculature, and cerebral vessels with high signal to background ratios was performed *via* NIR-II imaging; Moreover, PA imaging has also been performed to clearly observe tumors *in vivo*. These results demonstrate that by finely tuning molecular aggregation in DTPA-TBZ, a good NIR-I absorptivity and a highly emissive fluorescence in the NIR-II region can be achieved simultaneously, finally resulting in a promising dual-modal imaging platform for real-world applications to achieve precise cancer diagnostics.

Introduction

Over the past few decades, cancer therapy has become a hot topic of social concern because of its beneficial use in treating patients affected by tumors. For cancer therapy, early diagnosis, tumor metastasis monitoring, and then surgery are three basic but indispensable processes. Interestingly, they all require efficient imaging techniques and instruments to achieve their goals during the treatment. Among the reported and commercialized imaging techniques, a rather good performance, such as infinite penetration in several cases, can be achieved for computed tomography (CT), positron emission tomography (PET), magnetic resonance imaging (MRI), and ultrasound imaging (US). However, disadvantages, such as the use of harmful ionization energy sources in CT and PET, an inferior spatial resolution in MRI, US, and PET, and a long collection time in MRI and CT, can also be observed. Therefore, it is urgent to develop more improved and facile imaging techniques. Fluorescence imaging exhibits several advantages, such as a fast and sensitive response, and a high temporal resolution. Moreover, it is a non-invasive process. For these reasons, it has recently received tremendous attention.[1] In the fluorescence imaging field, near infrared (NIR) imaging,[2] including NIR-I (700–900 nm) and NIR-II (1000–1700 nm), is usually considered the most promising alternative to conventional imaging techniques because of its deep tissue penetration, minimal photo-damage, and clear but facile visualization when compared to short-wave fluorescence imaging (<700 nm). However, although high photoluminescence quantum yields (PLQYs) and imaging instruments can be easily obtained for fluorophores in the NIR-I region (700–900 nm), limitations of light scattering and auto-fluorescence for biological tissues in this region still partially existed. Therefore, fluorescence in a second window (NIR-II, 1000–1700 nm) with significantly reduced photo scattering and faint tissue auto-fluorescence exhibits a larger potential, which is also considered an ideal imaging modality for real-time biological

*a*School of Chemistry, MOE Key Laboratory for Non-equilibrium Synthesis and Modulation of Condensed Matter, Xi'an Key Laboratory of Sustainable Energy Material Chemistry, Xi'an Jiao Tong University, Xi'an 710049, P. R. China. E-mail: dongfengdang@xjtu.edu.cn; menglingjie@xjtu.edu.cn

*b*Guangdong Key Laboratory of Nanomedicine, CAS Key Laboratory of Health Informatics, Shenzhen Bioactive Materials Engineering Lab for Medicine, Institute of Biomedicine and Biotechnology, Shenzhen Institutes of Advanced Technology, Chinese Academy of Sciences, Shenzhen, 518055, P. R. China. E-mail: pf.zhang@siat.ac.cn

*c*Instrumental Analysis Center, Xi'an Jiao Tong University, Xi'an, 710049, P. R. China
† Electronic supplementary information (ESI) available: Experimental section, NMR, mass and absorption spectra, cell viability, cell imaging, fluorescence mapping spectra, and the QY of DTPA-TBZ. See DOI: 10.1039/d0sc03160g

imaging and visualization with deep penetration and high temporal resolution.[3]

In the second window fluorescence imaging, NIR-II fluorophores affect the imaging performance significantly. Thus, much more attention has been recently paid to the preparation of new NIR-II fluorophores. So far, numerous inorganic NIR-II fluorophores, including carbon nanotubes (CNTs),[4] quantum dots (QDs),[5] and rare-earth doped nanoparticles,[6] have been reported to achieve efficient high resolution in deep tissues and tumor imaging. In addition, organic fluorophores and their fluorescence nanoparticles have also been recently used in NIR-II imaging because of their tunable chemical structures, photophysical characteristics, simple processability, and excellent biocompatibility.[7] However, it is noted that most of the organic NIR-II fluorophores exhibit an inferior emission brightness due to the energy gap law. Moreover, only NIR-II fluorophores with high PLQYs can produce bright fluorescence signals and high signal to background ratios (S/B) in deep tissues due to the inevitable drop of excitation power. Therefore, novel NIR-II organic fluorophores with an ultra-high brightness must be developed.

Currently, much more effort has been devoted to acquiring highly emissive organic NIR-II fluorophores.[8] For instance, Dai *et al.* reported a NIR-II organic fluorophore of p-FE, which has an impressively high emission efficiency of 16.5%.[9] However, despite the significant progress, the aggregation-caused quenching (ACQ) phenomenon in some traditional dyes, such as 4-[2-[2-chloro-3-[2-(2-phenylthiochromen-4-yl)ethenyl]-1-cyclohex-2-enylidene]ethyl-idene]-2-phenyl-thiochro-mene (IR 26), should be prevented. These dyes usually display a weak or almost no emission in aggregated states caused by the ACQ, significantly hindering their biological applications. Another issue for organic NIR-II fluorophores is the large cross-talk between their absorption spectra and photo-luminescence spectra, resulting in small Stokes' shifts and high self-absorption, finally also leading to an inferior fluorescence brightness. To solve these problems, Tang and his co-workers proposed an "aggregation-induced emission" (AIE) concept.[10] By following this concept, AIE luminogens (AIEgens) and their corresponding nanoparticles (also known as AIE dots) were tremendously developed.[11] These materials exhibit non- or weak emission in solution, but emit brightly in aggregated states. This results in a deeper penetration and higher temporal resolution in real-time biological imaging, such as NIR-II imaging. Interestingly, large Stokes' shifts and impressive photo-stability can also be observed for AIEgens and AIE dots,[12] which are both beneficial for the visualization process in biological research. Recently, Tang and Qian *et al.* reported an organic NIR fluorophore of TQ-BPN with significantly high AIE features: an intense emission can be observed in the 700–1200 nm range and a high PLQY of 2.8% was obtained in the short-wave infrared region (SWIR, >900 nm). This value is much higher than those reported PLQYs for CNT SWIR emitters (PLQYs ≈ 0.4%), leading to the direct visualizing of brain vasculature with a high spatial resolution (≈3 μm) and a deep penetration (800 μm).[13] In another case, a NIR-II organic AIEgen based on HLZ-BTED was developed by Hong and his co-workers. It exhibits

outstanding fluorescence properties, high photo-stability and also has an excellent biocompatibility, indicating the biomedical applications of long-term breast tumor imaging and hind limb vasculature.[14] Additionally, Xiao's group recently developed HL3-based AIE dots for NIR-II, NIR-IIa, and NIR-IIb imaging, where HL3 dots exhibited a remarkably enhanced fluorescence intensity with a PLQY of 11.7% in the NIR-II window (>1000 nm) and 0.05% in the NIR-IIb region (>1550 nm), finally resulting in impressive high-resolution *in vivo* imaging.[15] The same group also reported AIE dots of HQL2 with high brightness to achieve high performance NIR-IIa and NIR-IIb vascular imaging.[16] However, it should be mentioned that although significant progress has been achieved in the development of NIR-II fluorophores, their inherent penetration depth in fluorescence imaging is always a questionable issue even for AIE dots in NIR-II imaging due to the limited spatial resolution. Fortunately, this problem can be solved by integrating another imaging technique, such as photoacoustic (PA) imaging, which usually exhibits low scattering characteristics. The use of ultrasound as the signal source provides a good spatial resolution in deep tissues and can perfectly compensate for the disadvantages of fluorescence imaging (Fig. 1A).[17] Zheng and Liu *et al.* reported a NIR-II fluorescent molecule TB1 with good AIE properties for a high PLQY of up to 6.2% and also
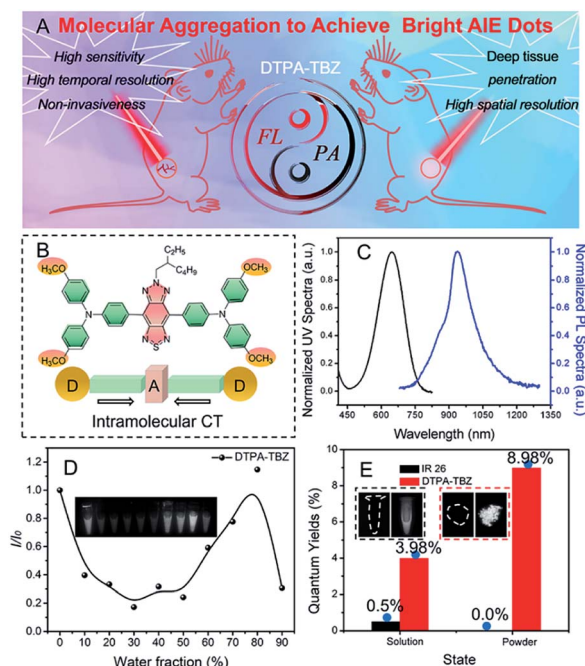

Fig. 1 Schematic illustration of DTPA-TBZ for dual NIR-II fluorescence imaging (FL) and NIR-I photoacoustic imaging (PA) *in vivo* (A); chemical structure of DTPA-TBZ (B); UV-Vis (black) and PL (blue) spectra of DTPA-TBZ in tetrahydrofuran (THF, [c] = 1 × 10⁻⁵ M) (C); relative PL intensity (I/I_0) of DTPA-TBZ in a THF/water mixture with different water fractions. The inset shows their corresponding fluorescence images (D); absolute PLQYs of IR 26 and DTPA-TBZ in the dilute solution and powder state (E). The inset shows the fluorescence images of IR-26 and DTPA-TBZ in a dichloroethane (DCE) solution (black dashed line) and a solid powder (red dashed line) under 808 nm illumination.

a large NIR absorptivity. Encouragingly, such developed TB1-based AIE dots were initially used in dual-modal imaging in NIR-II fluorescence and NIR-I PA imaging for precise brain cancer diagnostics.[18]

Despite the tremendous achievement, bright AIEgens or AIE dots with high PLQY values in the NIR-II region are still limited currently (Scheme S1 and Table S1, ESI†). Therefore, the further improvement and enhancement of their fluorescence performance in the NIR-II region remain an open point. Although it is known that intramolecular motion restriction during the aggregation process is highly important to define the fluorescence performance in AIEgens, few studies were reported in this field since most of these processes are subject to natural characteristics. Based on this consideration, in this work, a new donor–acceptor (D–A) tailored NIR-II emissive AIEgen called DTPA-TBZ (Fig. 1B) was developed to fine-tune molecular aggregation in nanoparticles and enhance their fluorescence performance. Benefiting from its D–A typed molecular framework, DTPA-TBZ exhibits an excellent absorptivity in the low-energy band (2.51×10^4 L mol^{-1} cm^{-1} at 648 nm), improving its NIR-I PA imaging capability. Moreover, it displays fluorescence signals in the NIR-II region with an emission up to 1200 nm. In contrast to DTPA-TBM, which is based on the same D–A framework but with only one methyl group, an enhanced molecular aggregation and intramolecular motion restriction can be observed for DTPA-TBZ by theoretical calculation, and thus good AIE characteristics and enhanced fluorescence performance with a high absolute PLQY of 8.98% in aggregated states were achieved in this case. Interestingly, the absolute PLQY value of DTPA-TBZ in the region >900 nm also reaches 6.69%. By encapsulating the prepared DTPA-TBZ within an amphipathic and tumor-specific FA-DSPE-PEG2000 molecule, the corresponding AIE dots with a high fluorescence QY of 11.1% (relative to IR 26 of 0.5%) in the region >900 nm were prepared and a PLQY value of 2.7% was calculated in the NIR II window (>1000 nm). To the best of the authors' knowledge, this compound here exhibits one of the most impressive PLQY values among AIE dots with NIR-II emission. Due to their excellent absorption in the NIR I region and fluorescence performance in the NIR II window, DTPA-TBZ-based AIE dots were finally used for dual modal imaging in NIR-II fluorescence imaging and NIR-I PA imaging. For NIR-II fluorescence imaging, a much higher S/B value can be observed than the one measured in the NIR-I region. Moreover, a detailed visualization of abdominal vessels, hind limb vasculature, and cerebral vessels was achieved. In addition, tumor imaging in BALB/c nude mice was also conducted by using DTPA-TBZ-based AIE dots in the NIR-II region. The results clearly show the tumor boundary via an accumulation process. Furthermore, time-dependent PA imaging via hypodermic injection can also be achieved to observe the uniform distribution of AIE dots inside the tumor, suggesting the deep penetrating ability of PA imaging. These results finally demonstrate that by finely tuning molecular aggregation, highly emissive fluorescence characteristics with an impressive PLQY value can be easily achieved for DTPA-TBZ-based AIE dots. Moreover, this compound exhibits a good absorptivity in the NIR-I region, and can be used in both high performance NIR-II fluorescence imaging and NIR-I PA imaging, enabling real-world applications, such as image-guided tumor surgery.

Results and discussion

Synthesis and optical properties

To produce the NIR-II AIEgen of DTPA-TBZ, a facile Suzuki coupling reaction was used with a yield of 78% (Fig. S1, ESI†) by employing the electron-donating triphenylamine (TPA) unit and an electron-withdrawing thiadiazolobenzotriazole (TBZ) core to form the donor–acceptor (D–A) molecular backbone. Here, an iso-octyl chain was attached to fine-tune molecular aggregation in solid states. The chemical structure of DTPA-TBZ is shown in Fig. 1B. This structure has been well characterized and confirmed via ^{1}H-NMR, ^{13}C-NMR, and high resolution mass spectrometry (ESI†). In addition, UV-Vis absorption and photoluminescence (PL) spectra of DTPA-TBZ in a THF solution ($[c] = 1 \times 10^{-5}$ M) were investigated. A broad absorption spectrum covering the 300–800 nm region was observed for DTPA-TBZ. The two absorption bands centered at 339 and 648 nm (Fig. 1C and S2 of the ESI†) can be attributed to the π–π^* transitions and the intramolecular charge transfer (ICT) between TPA units and the TBZ core,[19] respectively. In addition, the molar absorption coefficient for DTPA-TBZ in a THF solution was also measured and a large absorptivity of 2.51×10^4 L mol^{-1} cm^{-1} at 648 nm was observed (Fig. S3, ESI†). The UV-Vis absorption spectrum for DTPA-TBZ in the solid state also further indicates its remarkable light absorption ability (Fig. S4, ESI†). The DTPA-TBZ compound in solution was then photoexcited. The resulting PL spectrum covers the 750–1200 nm range and the maximum emission feature is located at 928 nm. These data demonstrate that efficient fluorescence signals can be observed for DTPA-TBZ in the NIR-II region, providing the possibility to perform real-time biological NIR-II imaging with a very high temporal resolution. Moreover, a large Stokes' shift of up to 280 nm in DTPA-TBZ was also achieved, implying that the self-absorption issue for conventional NIR-II fluorophores can be fully avoided here, finally resulting in a significantly enhanced fluorescence brightness.

To investigate the AIE performance of DTPA-TBZ, its PL spectrum in a mixture of THF/water with a varying water fraction (f_w) was then monitored (Fig. S5, ESI†) and the relative PL intensity (I/I_0) in mixed solvents is shown in Fig. 1D. Similar to other D–A structured fluorophores, when the f_w value increases from 0% to 50%, the fluorescence intensity decreases gradually due to the twisted intramolecular charge transfer (TICT),[20] which can also be demonstrated by the PL spectra in various solvents (Fig. S6, ESI†). However, when water is added to induce aggregation ($f_w = 50$–80%), the emission signal of DTPA-TBZ is largely intensified, showing a typical AIE characteristic.[20,21] When f_w is 90%, DTPA-TBZ can easily precipitate,[22] and thus an inferior emission performance is observed. Generally, a highly bright emission can be obtained for AIE-active molecules in aggregated states, such as the solid state, leading to their use in real-world biomedical imaging. Therefore, the PL spectrum of DTPA-TBZ in solids was measured (Fig. S7, ESI†), and it exhibits efficient fluorescence signals in the NIR-II region with an

emission extending to 1200 nm. The absolute PLQYs of DTPA-TBZ in a dilute solution and solid state were further investigated. Moreover, the commercial NIR-II dye of IR 26 was also measured as a reference. As anticipated, IR 26 displays a weak or almost no emission in both the solution and the aggregated state. Its absolute PLQYs are listed in Fig. 1E. In the case of DTPA-TBZ, emission in THF solution with a moderate absolute PLQY of 3.98% is observed, but a more enhanced fluorescence performance is observed in aggregated solid states because of its AIE features. Finally, ultra-high PLQYs of 8.98% in the whole range (Fig. 1E) and 6.69% in the >900 nm region were obtained, demonstrating that DTPA-TBZ can be a promising NIR-II imaging platform for real-time biological imaging and visualization. Furthermore, the transient decay spectra of DTPA-TBZ in dilute solution (Fig. S8, ESI†) and solid states (Fig. S9, ESI†) were also recorded. Their corresponding lifetime (τ), calculated radiative decay rates (k_r), and nonradiative decay rates (k_{nr}) are listed in Table S2.†[23] The data showed that although the k_r values are similar for DTPA-TBZ in both solution and solid states, a much smaller k_{nr} value is observed in the solid state, indicating that the non-radiative decay channel can be well blocked in solids, and thus impressive fluorescence performance for solid-stated DTPA-TBZ can be finally achieved.

Preparation and optical properties of AIEdots

To further enhance its water dispersity and biocompatibility, a nano-precipitation strategy was employed by encapsulating DTPA-TBZ into an amphipathic and tumor-specific matrix (FA-DSPE-PEG2000).[24] The chemical structure of FA-DSPE-PEG2000 is shown in Fig. S10 (ESI†). The preparation of DTPA-TBZ-based AIE dots is outlined in Fig. 2A. Commonly, three basic factors were considered to tune the size in prepared AIE dots: (1) initial concentration of fluorophores in solution, (2) volume ratios between THF and water, and (3) amphiphilic block copolymers utilized for modifying AIE dots.[25] According to our previously published work, the optimized preparation for DTPA-TBZ-based AIE dots is finally determined (ESI†).[25] Their particle size and zeta potential were then investigated at pH = 7.4 *via* dynamic light scattering (DLS). A hydrodynamic diameter of ∼143 nm, a polydispersity index (PDI) value of 0.16, and a zeta potential of −34.90 mV were obtained. Moreover, nano-spheres with an average size of ∼50 nm were observed by using a transmission electron microscope (TEM), and the distribution of particle size for the prepared AIE dots by TEM was also calculated and is shown in Fig. S11† (ESI†), which demonstrated their monodisperse properties. These appropriate particle sizes here also imply their potential applications for cell uptake and imaging (Fig. 2B). UV-Vis absorption and PL spectra of the DTPA-TBZ-based AIE dots were also measured (Fig. 2C) and similar to their solution-state profiles, efficient absorption and emission spectra located at 652 nm and 929 nm, respectively, were observed. Interestingly, the DTPA-TBZ-based AIE dots exhibit a good NIR-I absorptivity with a large molar extinction coefficient of 462.2 L g^{-1} cm^{-1} at 646 nm (Fig. S12, ESI†). Also, a coefficient of ∼19.4 L g^{-1} cm^{-1} at 808 nm was observed, indicating their great potential in NIR-I PA imaging and NIR-II
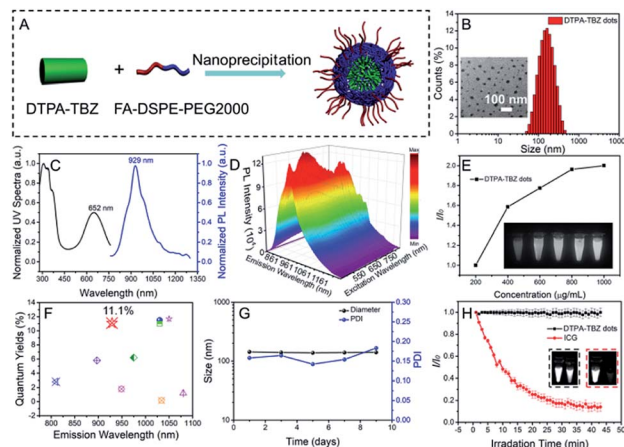

Fig. 2 Schematic illustration of the preparation process of DTPA-TBZ-based AIE dots (A); DLS data of DTPA-TBZ-based AIE dots. The inset shows their corresponding TEM images (B); UV-Vis absorption and PL spectra of the DTPA-TBZ-based AIE dots (C); PL-excitation mapping of the DTPA-TBZ-based AIE dots in an aqueous dispersion (D); fluorescence signals of the DTPA-TBZ-based AIE dots with different concentrations. The inset shows their corresponding fluorescence images under 808 nm excitation (E); PLQYs of the DTPA-TBZ-based AIE dots and other reported NIR-II fluorophores (F); size and PDI stability of the DTPA-TBZ-based AIE dots (G); photo-stability of ICG and the DTPA-TBZ-based AIE dots after continuous laser irradiation (808 nm, 1 W cm^{-2}). The inset shows the fluorescence images of DTPA-TBZ-based AIE dots (left) and ICG (right) before (black line) and after (red line) the irradiation process (H).

fluorescence imaging. In addition, the PL spectra of AIE dots in aqueous solution at various pH values were also investigated and are displayed in Fig. S13 (ESI†), and their fluorescence intensities are shown in Fig. S14 (ESI†). It is found that highly emissive signals were observed for the developed AIE dots at different PH values, thus leading to a great potential in biological imaging. The transient decay spectra of DTPA-TBZ-based AIE dots were also measured (Fig. S15, ESI†), showing a calculated lifetime of ∼1.14 ns. Furthermore, PL excitation mapping in three-dimension (3D) was carried out to gain an in-depth understanding of the excitation–fluorescence relation for DTPA-TBZ-based AIE dots. An excitation/emission peak located at ≈652/929 nm and an obvious emission signal at 1000 nm can be observed (Fig. 2D and S16 of the ESI†). In addition to the AIE curves (Fig. 1D), AIE features of the prepared dots were further investigated by varying their concentration. As expected, when the concentration increases, the observed emission signals *via* the NIR-II fluorescence imaging system improve obviously (excited at 808 nm, Fig. 2E), further demonstrating their good AIE characteristics. Furthermore, the relative PLQYs of DTPA-TBZ-based AIE dots and of several other reported NIR-II fluorophores were also recorded (Fig. 2F).[11a,j,13,14,18,26] The AIE dots investigated in this work report a PLQY of 11.1% (>900 nm) under 808 nm excitation with the IR-26 dye as a reference (PLQY = 0.5%), according to a published protocol (Fig. S17, ESI†).[18,27] Encouragingly, the PLQY of AIE dots here in the NIR II window (>1000 nm) is 2.7% (Fig. S18, ESI†). It should be mentioned that although similar methods were used, the PLQY value of DTPA-

TBZ is much higher than most of the values reported for other organic NIR-II fluorophores (Fig. 2F and Table S1, ESI†). To the best of the authors' knowledge, this is one of the most impressive PLQY values for prepared AIE dots with NIR-II features and such emission characteristics further demonstrate the capabilities of DTPA-TBZ-based dots in high performance NIR-II fluorescence imaging. The size stability and photo-stability of DTPA-TBZ-based AIE dots were then recorded (Fig. 2G and H). Interestingly, highly stable features were observed over 10 days, including unchanged hydrodynamic diameters and PDI values. Additionally, the photo-stability of DTPA-TBZ-based AIE dots was also measured and compared. For commercial dyes, such as indocyanine green (ICG), the fluorescence is almost completely quenched under continuous laser irradiation at 808 nm with a power density of 1 W cm^{-2} for 40 min. However, a similar fluorescence intensity without an obvious signal loss was observed in DTPA-TBZ-based dots, indicating their high resistance to photo-bleaching (Fig. 2H). The excellent fluorescence characteristics and impressive stability of the DTPA-TBZ-based AIE dots further demonstrate their potential in high performance NIR-II fluorescence imaging and long-term monitoring in biological research.

Theoretical calculation

To further understand the bright emission of DTPA-TBZ-based AIE dots, density functional theory (DFT) calculations were carried out. DTPA-TBM containing the same molecular backbone as DTPA-TBZ but having a methyl group was introduced as the model compound (Fig. S1, ESI†). Based on the optimized geometries from DFT calculations at the B3LYP/6-31G (d, p) level, both DTPA-TBM and DTPA-TBZ exhibit a twisted molecular conformation along the backbone. Especially in the case of DTPA-TBZ, large dihedral angles up to ~68.37° between adjacent aromatic rings are observed (Fig. 3A and C). This torsional molecular backbone can efficiently prevent the molecular π–π stacking, thus contributing to the enhanced emission efficiency in DTPA-TBZ.[28] Additionally, the highest occupied molecular orbital (HOMO) and the lowest unoccupied molecular orbital (LUMO) were also investigated and similar electronic structures were obtained for both DTPA-TBM and DTPA-TBZ: the HOMO is delocalized on both the donor and acceptor units, whereas the LUMO is only distributed on the electron-deficient acceptor (Fig. 3B and D), suggesting the existence of efficient ICT interactions.[29] In contrast to DTPA-TBM, the large band gap of DTPA-TBZ (calculated via DFT) caused by its decreased molecular conjugation further demonstrates its twisted backbone. This result is also in good agreement with the findings in Fig. 3A and C. Molecular dynamics (MD) simulations (25 ns) were also conducted to investigate the effect of molecular structures on their molecular aggregation.[30] Initially, the snapshots of geometries for DTPA-TBM and DTPA-TBZ, including the single molecule (Fig. 3E) and aggregates (Fig. 3F), were captured via MD simulations. The distribution of dihedral angles in aromatic rings for DTPA-TBM and DTPA-TBZ was also displayed (Fig. S19 and S20, ESI†), respectively. It is observed that similar to the DFT calculation results, both molecules display twisted
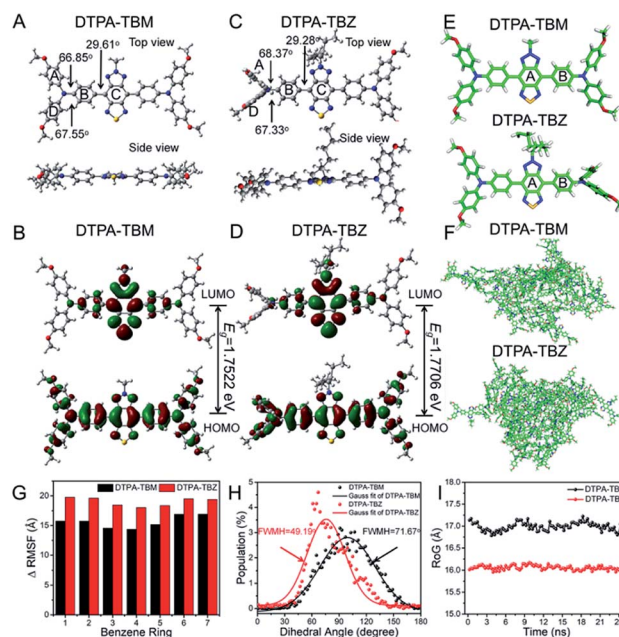

Fig. 3 Geometries of DTPA-TBM and DTPA-TBZ optimized via DFT at the B3LYP/6-31G (d, p) level ((A and C) including top view and side view); electron density distribution of molecular orbitals in DTPA-TBM and DTPA-TBZ ((B and D) including HOMO and LUMO); snapshots of the geometries of DTPA-TBM and DTPA-TBZ in the single molecule (E) and aggregates (F) obtained via the MD simulations; the decreased RMSF values of each phenyl ring over MD simulations (G) for DTPA-TBM and DTPA-TBZ in the single molecule and aggregates; dihedral angle distribution between phenyl rings A and B (H) for DTPA-TBM and DTPA-TBZ in aggregates; RoG values (I) for the geometries of DTPA-TBM and DTPA-TBZ in aggregates.

molecular structures in MD calculation. To confirm the enhanced molecular aggregation in DTPA-TBZ, the root mean square fluctuation value (RMSF) was firstly used to illustrate the vibrations and rotations of molecules. RMSF values for each phenyl ring in both DTPA-TBM and DTPA-TBZ are listed in Fig. S21 (ESI†), including the single molecule and aggregates. The decreased values from the single molecule to aggregate states for both DTPA-TBM and DTPA-TBZ were also compared in Fig. 3G. When passing from single molecules to aggregates, although a similar changing trend is observed, the recorded RMSF values show a larger decrease for DTPA-TBZ. This demonstrates that intensive packing and aggregation occur in DTPA-TBZ. Successively, the dihedral angle distribution functions of the DTPA-TBM and DTPA-TBZ in aggregate states were compared and their corresponding FWHM values were also recorded (Fig. 3H). DTPA-TBM with the methyl group shows a broad dihedral angle distribution in the range of 40–160° (120°) between the phenyl ring A and B in aggregates (black line). However, in the case of DTPA-TBZ, although only the side chain changes into an octyl group, a much narrowed dihedral angle distribution is observed for the same phenyl rings (red line). The calculated FWHM value for DTPA-TBZ is only 49.19°, which is much smaller than that in DTPA-TBM (71.67°), indicating that the molecules in DTPA-TBM can easily move and rotate even in the aggregated state, whereas this molecular

flexibility is limited in DTPA-TBZ due to its enhanced molecular packing and aggregation, thus providing enhanced fluorescence performance in AIEgens. Furthermore, the RoG values were also employed to estimate the structural flexibility of DTPA-TBM and DTPA-TBZ. As displayed in Fig. 3I, both molecules are probably packed in a disordered manner: their RoG values are ~17.0 and 16.0 Å, respectively. However, the low RoG value of DTPA-TBZ further implies its intensive aggregation tendency. For this reason, according to the RIM mechanism in AIE research, its non-radiative pathways can be efficiently blocked, thus leading to an enhanced fluorescence efficiency in its aggregated state, even in the NIR-II region. These results illustrate an efficient strategy to fine-tune molecular aggregation in aggregates through alkyl chain engineering, which results in highly bright NIR-II AIE dots and they can be used in real-time fluorescence imaging with high resolution.

In vivo fluorescence imaging

To demonstrate the use of DTPA-TBZ-based AIE dots as NIR-II *in vitro* and *in vivo* imaging agents, their biocompatibility and cytotoxicity were assessed by using LO_2 and 4T1 cells *via* a standard WST-1 cell proliferation and cytotoxicity assay kit. After incubation with DTPA-TBZ-based AIE dots for 24 h and 48 h, respectively, a cell viability of 85% can be observed for both cells even at a high concentration of 25 μg mL^{-1}. This indicates their good biocompatibility and low cytotoxicity (Fig. S22 and S23, ESI†). Cell imaging using the developed AIE dots was also conducted *via* confocal laser scanning microscopy (CLSM). The procedure for cell imaging is also listed (ESI†). Initially, 4′,6-diamidino-2-phenylindole (DAPI) was used to localize HeLa cells with an excitation wavelength of 405 nm. Successively, bright fluorescence signals appeared after incubation with DTPA-TBZ-based AIE dots with a low concentration of 4 μg mL^{-1} under 650 nm excitation. Similar to other AIE dots, the fluorescence signals mainly appear in the cell cytoplasm (Fig. S24, ESI†), illustrating the high cell uptake of AIE dots and showing their potential for fluorescence *in vivo* imaging.

Since DTPA-TBZ exhibits a broad emission spectrum in both the NIR-I region and the NIR-II region, the developed AIE dots were simultaneously used in NIR-I and NIR-II fluorescence *in vivo* imaging. Initially, a long-term tumor in BALB/c mice *via* hypodermic injection was tracked in the NIR-I fluorescence window by using DTPA-TBZ-based AIE dots (1 mg mL^{-1}, 40 μL). The fluorescence was recorded using noninvasive live-animal imaging. As shown in Fig. 4A, the fluorescence signals from the 4T1-bearing tumor under 640 nm excitation were monitored *in situ* over 15 days. Interestingly, bright fluorescence signals can be observed during the whole process, and their calculated mean fluorescence intensity demonstrates that DTPA-TBZ-based AIE dots can be used for long-term tracking and monitoring in biological research (Fig. S25, ESI†). Then, *in vivo* fluorescence imaging results in the NIR-I region and NIR-II region were compared (Fig. 4B–D). Since the light scattering and the auto-fluorescence for biological tissues in the NIR-I region can still be observed, a spatial resolution with an inferior signal-to-background ratio
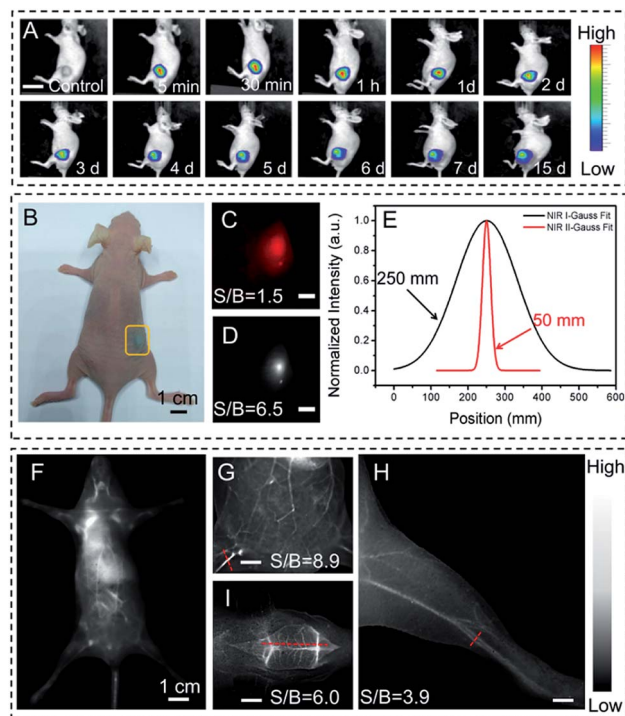

Fig. 4 Long-term tumor tracking in the NIR-I fluorescence window in BALB/c nude mice bearing the 4T1-tumor *via* hypodermic injection using DTPA-TBZ-based AIE dots, scale bar 2 cm; (A); bright field of BALB/c nude mice bearing the 4T1-tumor *via* hypodermic injection using DTPA-TBZ-based AIE dots (B); signal-to-background values for tumor imaging in the NIR-I region under 650 nm excitation (C) and in the NIR-II region under 808 nm excitation (D), scale bar = 50 mm; Gaussian fit of the fluorescence intensity profile (E) in NIR-I (black line) and NIR-II (red line) regions with the calculated FWHM values; fluorescence images of BALB/c nude mice in the NIR-II region by intravenous injection of DTPA-TBZ-based AIE dots (F); enlarged view of the abdominal vasculature imaging (G), hind limb vasculature imaging (H), and cerebral vessel imaging (I) by using DTPA-TBZ-based AIE dots in the NIR-II region, scale bar = 400 μm.

(S/B) of 1.5 was only observed (Fig. 4C). However, such poor imaging resolution can be fully avoided by using an InGaAs camera (Fig. 4D). In this case, a much higher S/B value of up to 6.5 in the NIR-II region can be achieved. In addition, the Gaussian fit of the fluorescence intensity profile in both the NIR-I and NIR-II regions provides their corresponding full-width at half maximum (FWHM) values. A FWHM value of only 50 mm was achieved in the NIR-II region for the DTPA-TBZ-based AIE dots due to their impressive NIR-II emission features (Fig. 4E). *In vivo* imaging of BALB/c nude mice in the NIR-II region *via* the intravenous injection of DTPA-TBZ-based AIE dots (1 mg mL^{-1}) was also performed by using a 1000 nm LP filter (Fig. 4F). After the injection, fluorescence signals can be immediately observed in the whole mice body, even in the blood vessels, indicating the great potential of DTPA-TBZ as a NIR-II imaging agent. Since the fluorescence in the second window exhibits a reduced photo-scattering effect and a faint tissue auto-fluorescence, it can be used for real-time biological imaging with deep penetration. Here, as a proof-of concept, a standard tissue phantom measurement was carried out to

estimate the tissue penetration depth of DTPA-TBZ-based AIE dots (1 mg mL^{-1}) in the NIR-II region by using a commercially available intralipid solution.[31] The fluorescence images were captured by increasing the concentration of intralipid from 0% to 1.8% to approximate the tissue lipid content in the mice body. It should be mentioned that although the emission intensity decreases gradually due to the high concentration of intralipid, the fluorescence images can still be clearly captured with a high image integrity since the high PLQY in the NIR-II window minimizes the photo-scattering (Fig. S26, ESI†). Finally, a quantitative analysis of the tissue penetration at a depth of 0.95 cm was achieved by using the DTPA-TBZ-based AIE dots (Fig. S27, ESI†). Based on the significant emissive features in the NIR-II region and the high penetration depth of the DTPA-TBZ-based AIE dots, abdominal and hind limb vasculatures were well imaged by exciting the tissue with an 808 nm diode laser (1 W cm^{-2}). The data were also collected *via* a 1000 nm LP filter with an exposure time of 70 ms. Interestingly, after injection of the highly emissive AIE dots, the abdominal vessels can be clearly identified by using NIR-II fluorescence imaging with a high S/B value of 8.9 (Fig. 4G). The cross-sectional intensity profile along the red-dashed line in Fig. 4G is also curved, leading to a sharp peak with a narrowed FWHM value of 73 μm (Fig. S28, ESI†). By using the DTPA-TBZ-based AIE dots, the hind limb vasculature can also be easily imaged with a high resolution (Fig. 4H, S/B = 3.9). The fusion and fission of vessels in the hind limb can be well visualized through the intact skin (Fig. 4H), which can also be confirmed by the Gaussian fitted fluorescence intensity curves (Fig. S29, ESI†). Additionally, the blood vessels in the mice brain were visualized through the skull. As displayed in Fig. 4I, the cerebral vessels can be observed distinctly with a high S/B value of 6.0. Small diameters of 100 μm for the cerebral vessels were also obtained according to the FWHM values in Gaussian fitted fluorescence intensity curves (Fig. S30, ESI†). These results demonstrate that, benefiting from their highly bright emission in the NIR-II region, the DTPA-TBZ-based AIE dots are a promising NIR-II imaging agent in real-time deep tissue imaging with a high S/B value and temporal resolution.

Tumor imaging is highly important for its early diagnosis, monitoring and also surgery in cancer therapy. Therefore, here tumor imaging in BALB/c nude mice was also conducted by using DTPA-TBZ-based AIE dots in the NIR-II region. The data were collected *via* an InGaAs camera. As shown in Fig. 5, after the intravenous injection of DTPA-TBZ-based dots (1 mg mL^{-1}) into the tumor-bearing nude mice, the fluorescence features generated by AIE dots can be gradually monitored at the tumor site through an accumulation process: the tumor becomes brighter as the time elapses. This accumulation process can be easily understood due to the passive targeting of the enhanced permeability retention (EPR) effects,[32] and active targeting ability of folic acid in DTPA-TBZ-dots. The average fluorescence intensity in the tumor was also collected (Fig. S31, ESI†). To further understand the accumulation process of DTPA-TBZ-dots, the major organs in nude mice, such as the heart, liver, lung, spleen, kidney, and the tumor, were also collected and imaged by using a NIR-II imaging
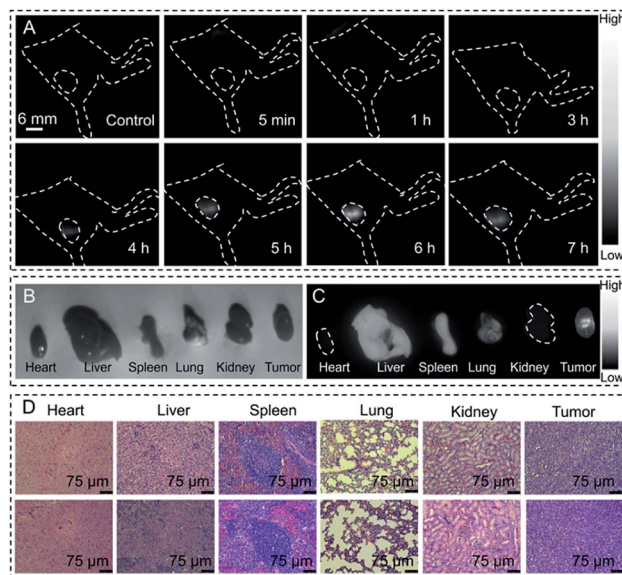

Fig. 5 Time-dependent tumor imaging in BALB/c nude mice bearing the 4T1-tumor using the DTPA-TBZ-based AIE dots over 7 h in the NIR-II region. The excitation wavelength of the laser diode is 808 nm with a power density of 1 W cm^{-2}. The dashed circle indicates the subcutaneous 4T1 tumor (A); the bright field image (B) and fluorescence image acquired using the NIR-II imaging system (C) for major organs and the tumor in BALB/c nude mice; histopathology examination of major organs and the tumor in BALB/c nude mice ((D) top: the mice were injected with PBS; down: the mice were injected with the DTPA-TBZ-based AIE dots).

system (Fig. 5B and C). The result shows that in addition to the tumor, the fluorescence signals can also be observed in the liver and spleen due to their metabolic functions. The histopathology examination of these organs was further performed to estimate the biocompatibility of AIE dots *in vivo*. As displayed, post-injection of DTPA-TBZ-based AIE dots, no obvious inflammation or abnormalities in the major organs of the mice were observed (Fig. 5D). The main hematology indicators for the nanoparticles in blood circulation, including the mean corpuscular hemoglobin (MCH), the mean corpuscular hemoglobin concentration (MCHC), the mean corpuscular volume (MCV), and hemoglobin (HGB), were also analyzed (Fig. S32, ESI†). Similar to the control sample that was injected with a PBS solution (pH = 7.4), no abnormity was found in the blood parameters, indicating that the DTPA-TBZ-based AIE dots also exhibit an excellent biocompatibility *in vivo*.

Photoacoustic imaging

Since the DTPA-TBZ-based AIE dots exhibit a good absorptivity in the low energy region, as a proof-of concept, their capability in NIR-I PA imaging was studied here. The PA imaging ability of AIE dots in a centrifugal tube under different wavelengths (Fig. S33, ESI†) was verified. As displayed, PA signals in the 650–850 nm range can be observed and the maximum PA signal is located mainly at 790 nm. Therefore, PA mapping of the DTPA-TBZ-based dots in a tube with different concentrations was determined at 790 nm (Fig. 6A) to produce a linear fit curve of
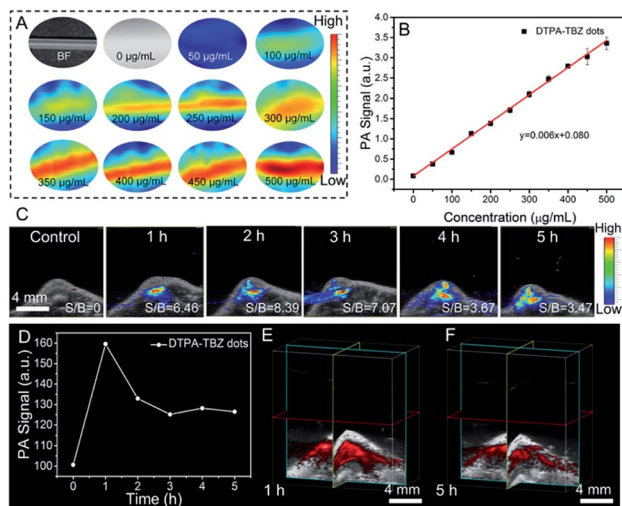
Fig. 6 PA mapping of the DTPA-TBZ-based AIE dots in a tube with different concentrations (A); linear fit curve of the PA intensity for DTPA-TBZ-based AIE dots with different concentrations (B); time-dependent PA imaging (C) and their signal intensity in the 4T1-tumor in BALB/c nude mice *via* hypodermic injection using DTPA-TBZ-based AIE dots (D); 3D view of the PA images in the tumor by using the DTPA-TBZ-based AIE dots ((E) 1 h; (F) 5 h).

PA signals (Fig. 6B). The proportional relation demonstrates that the AIE dots are truly a promising PA imaging candidate and can be used as a dual-modal imaging agent for NIR-II fluorescence and NIR-I PA imaging. Meanwhile, the PA properties of DTPA-TBZ based AIE dots and some reported PA reagents are summarized in Table S3 (ESI†). As is shown, the DTPA-TBZ-based AIE dots exhibit excellent light absorption ability, thus affording favorable PA imaging performance. The PA imaging performance by using DTPA-TBZ-based AIE dots was then investigated *in vivo* in BALB/c mice bearing a 4T1 tumor *via* hypodermic injection (1 mg mL^{-1}). Time-dependent PA imaging in the tumor is displayed in Fig. 6C. As can be observed, a uniform distribution of the prepared AIE dots inside the tumor is achieved after the *in situ* injection, suggesting the deep penetration ability of DTPA-TBZ-based dots in PA imaging. Furthermore, the PA imaging in the tumor also offers high signal/background ratios (3.4–8.4). According to the PA imaging in Fig. 6C, the mean intensity in the tumor over 5 h was also curved (Fig. 6D). The results demonstrate that the developed AIE dots can also be employed in long-term tracking by using the PA imaging modality. In addition, the PA images in 3D mode are reconstructed in Fig. 6E and F, showing well distributed PA signals in the 4T1 tumor with high spatial resolution. The tumors imaged by NIR-I imaging, NIR-II imaging, and 3D PA imaging were then fully compared (Fig. S34, ESI†) and it was observed that the inferior penetration depth in fluorescence imaging can be well solved in PA imaging due to the low scattering characteristics, resulting in a clear tumor boundary and depth. According to these results here, it can be concluded that DTPA-TBZ-based AIE dots can not only be well used in NIR-I/NIR-II fluorescence imaging, but also efficiently applied in PA imaging with high spatial resolution. They offer

a complementary imaging modality to acquire comprehensive information in future tumor diagnosis.

Experimental

Materials

FA-DSPE-PEG2000 was purchased from Ruixi Chemical Reagent Co. Ultrapure water (18.2 MΩ cm^{-1}) was used for all the experiments requiring an aqueous medium and was obtained from a Millipore Milli-Q purification system. Toluene and ethanol were purchased from Adamas Reagent Co., Ltd. (Shanghai, China). Other synthetic agents, such as *N,N*-bis(4-methoxyphenyl)-4-(4,4,5,5-tetramethyl-1,3,2-dioxaborolan-2-yl)-benzenamine, thiadiazolo-benzotriazole and Pd(PPh$_3$)$_4$, were purchased from TCI, Sigma-Aldrich or Energy Chemical (China) and used without additional purification unless specified otherwise.

Characterization and measurements

A Bruker Advance 400 MHz spectrometer was used to record the NMR spectra. CDCl$_3$ was employed as the solvent with tetramethylsilane as the internal standard (400 MHz for ^{1}H-NMR referenced to TMS at $\delta = 0.00$ ppm and 100 MHz for ^{13}C-NMR referenced to CDCl$_3$ at 77.00 ppm). High resolution mass spectrometry (HRMS) was performed on a Waters LCT Premier XE spectrometer. UV-Vis-NIR spectra were collected by using a Shimadzu UV-2250 spectrophotometer. The photoluminescence spectra and their absolute photoluminescence quantum yields (PLQYs) were measured using a FLS980 transient steady-state fluorescence spectrometer of Edinburgh Instruments. A Malvern Zetasizer Nano ZS90 was used to measure the hydrodynamic sizes, the PDI, and the zeta potential at room temperature. The morphology of AIE dots was imaged by using a HR-TEM electron microscope (JEOL-2100). The cell cytotoxicity was confirmed by using a WST-1 kit in a MD Spectra Max 190 microplate reader. The photoacoustic characterization was performed *via* an acoustic-resolution PA microscopy system of FujiFilm VisualSonics. The fluorescence imaging of the live animals in the NIR-I region was performed by using a Xenogen optical imaging system. The NIR-II fluorescence pictures were captured with a NIR-OPTICS Series III 900/1700 small animal imaging system (Suzhou NIR-Optics Technology Co., Ltd.) equipped with a 1000 nm long pass filter.

Conclusions

In conclusion, a D–A typed highly bright AIEgen of DTPA-TBZ was developed. This AIEgen does not only exhibit an excellent absorptivity in the NIR-I region, but also displays good fluorescence signals in the NIR-II region with the emission extending to 1200 nm. Interestingly, benefiting from the improved intramolecular restriction and aggregation in aggregates, DTPA-TBZ exhibits an impressively high absolute PLQY value of 8.98% in the solid state, which also reaches 6.69% in the >900 nm region. DTPA-TBZ-based AIE dots with a high fluorescence QY of 11.1% (relative to IR 26) were also prepared, leading to high resolution NIR-II fluorescence imaging in

visualization of abdominal vessels, hind limb vasculature, and cerebral vessels with high S/B values. In addition, the tumor imaging in BALB/c nude mice shows that a detailed visualization of the tumor boundary can be successfully achieved. Furthermore, PA imaging in a tumor can also be achieved *via* hypodermic injection even in the 3D mode to observe the uniform distribution of AIE dots inside the tumor. These findings imply that by finely tuning molecular aggregation in DTPA-TBZ, a good absorptivity in the NIR-I region and a highly emissive fluorescence in the NIR-II region can be achieved, providing a promising dual-modal imaging platform for future applications in cancer diagnostics.

Ethical statement

The animal experiments were carried out in compliance with the Animal Management Rules of Ministry of Health of the People's Republic of China. The animal treatments were in accordance with the protocols evaluated and approved by the Ethical Committee of Xi'an Jiao Tong University.

Conflicts of interest

There are no conflicts to declare.

Acknowledgements

Notes and references

1 (a) D. Ding, K. Li, B. Liu and B. Z. Tang, *Acc. Chem. Res.*, 2013, **46**, 2441; (b) O. S. Wolfbeis, *Chem. Soc. Rev.*, 2015, **44**, 4743; (c) K. Li and B. Liu, *Chem. Soc. Rev.*, 2014, **43**, 6570; (d) Z. Yang, A. Sharma, J. Qi, X. Peng, D. Y. Lee, R. Hu, D. Lin, J. Qu and J. S. Kim, *Chem. Soc. Rev.*, 2016, **45**, 4651; (e) L. Guo and M. S. Wong, *Adv. Mater.*, 2014, **26**, 5400; (f) S. Zhu, R. Tian, A. L. Antaris, X. Chen and H. Dai, *Adv. Mater.*, 2019, **31**, 1900321.

2 (a) K. G. Chernov, T. A. Redchuk, E. S. Omelina and V. V. Verkhusha, *Chem. Rev.*, 2017, **117**, 6423; (b) J. Zhao, D. Zhong and S. Zhou, *J. Mater. Chem. B*, 2018, **6**, 349; (c) V. Pansare, S. Hejazi, W. Faenza and R. K. Prud'homme, *Chem. Mater.*, 2012, **24**, 812; (d) Y. Cai, Z. Wei, C. Song, C. Tang, W. Han and X. Dong, *Chem. Soc. Rev.*, 2019, **48**, 22.

3 (a) H. Wan, H. Du, F. Wang and H. Dai, *Adv. Funct. Mater.*, 2019, **29**, 1900566; (b) C. Li and Q. Wang, *ACS Nano*, 2018, **12**, 9654; (c) F. Ding, Y. Zhan, X. Lu and Y. Sun, *Chem. Sci.*, 2018, **9**, 4370; (d) Y. Tang, F. Pei, X. Lu, Q. Fan and W. Huang, *Adv. Opt. Mater.*, 2019, **7**, 1900917; (e) S. He, J. Song, J. Qu and Z. Cheng, *Chem. Soc. Rev.*, 2018, **47**, 4258; (f) Z. Zhang, X. Fang, Z. Liu, H. Liu, D. Chen, S. He, J. Zheng, B. Yang, W. Qin, X. Zhang and C. Wu, *Angew. Chem., Int. Ed.*, 2020, **59**, 3691; (g) Kenry, Y. Duan and B. Liu, *Adv. Mater.*, 2018, **30**, 1802394; (h) C. Sun, B. Li, M. Zhao, S. Wang, Z. Lei, L. Lu, H. Zhang, L. Feng, C. Dou, D. Yin, H. Xu, Y. Cheng and F. Zhang, *J. Am. Chem. Soc.*, 2019, **141**, 19221.

4 (a) K. Welsher, S. P. Sherlock and H. Dai, *Proc. Natl. Acad. Sci. U. S. A.*, 2011, **108**, 8943; (b) K. Welsher, Z. Liu, S. P. Sherlock, J. T. Robinson, Z. Chen, D. Daranciang and H. Dai, *Nat. Nanotechnol.*, 2009, **4**, 773.

5 (a) A. Zebibula, N. Alifu, L. Xia, C. Sun, X. Yu, D. Xue, L. Liu, G. Li and J. Qian, *Adv. Funct. Mater.*, 2018, **28**, 1703451; (b) G. Hong, J. Robinson, Y. Zhang, S. Diao, A. Antaris, Q. Wang and H. Dai, *Angew. Chem., Int. Ed.*, 2012, **51**, 981.

6 (a) Y. Fan and F. Zhang, *Adv. Opt. Mater.*, 2019, **7**, 1801417; (b) M. Zhang, W. Zheng, Y. Liu, P. Huang, Z. Gong, J. Wei, Y. Gao, S. Zhou, X. Li and X. Chen, *Angew. Chem., Int. Ed.*, 2019, **58**, 9556.

7 (a) Q. Yang, Z. Hu, S. Zhu, R. Ma, H. Ma, Z. Ma, H. Wan, T. Zhu, Z. Jiang, W. Liu, L. Jiao, H. Sun, Y. Liang and H. Dai, *J. Am. Chem. Soc.*, 2018, **140**, 1715; (b) G. Xu, Q. Yan, X. Lv, Y. Zhu, K. Xin, B. Shi, R. Wang, J. Chen, W. Gao, P. Shi, C. Fan, C. Zhao and H. Tian, *Angew. Chem., Int. Ed.*, 2018, **57**, 3626; (c) Y. Tang, Y. Li, X. Lu, X. Hu, H. Zhao, W. Hu, F. Lu, Q. Fan and W. Huang, *Adv. Funct. Mater.*, 2019, **29**, 1807376; (d) J. Ouyang, L. Sun, Z. Zeng, C. Zeng, F. Zeng and S. Wu, *Angew. Chem., Int. Ed.*, 2019, **58**, 2; (e) H. Ma, C. Liu, Z. Hu, P. Yu, X. Zhu, R. Ma, Z. Sun, C. H. Zhang, H. Sun, S. Zhu and Y. Liang, *Chem. Mater.*, 2020, **32**, 2061; (f) S. Wang, J. Liu, G. Feng, L. G. Ng and B. Liu, *Adv. Funct. Mater.*, 2019, **29**, 1808365; (g) Y. Sun, M. Ding, X. Zeng, Y. Xiao, H. Wu, H. Zhou, B. Ding, C. Qu, W. Hou, A. Er-Bu, Y. Zhang, Z. Cheng and X. Hong, *Chem. Sci.*, 2017, **8**, 3489; (h) A. L. Antaris, H. Chen, S. Diao, Z. Ma, Z. Zhang, S. Zhu, J. Wang, A. X. Lozano, Q. Fan, L. Chew, M. Zhu, K. Cheng, X. Hong, H. Dai and Z. Cheng, *Nat. Commun.*, 2017, **8**, 15269.

8 (a) A. L. Antaris, H. Chen, K. Cheng, Y. Sun, G. Hong, C. Qu, S. Diao, Z. Deng, X. Hu, B. Zhang, X. Zhang, O. K. Yaghi, Z. R. Alamparambil, X. Hong, Z. Cheng and H. Dai, *Nat. Mater.*, 2016, **15**, 235; (b) B. Ding, Y. Xiao, H. Zhou, X. Zhang, C. Qu, F. Xu, Z. Deng, Z. Cheng and X. Hong, *J. Med. Chem.*, 2019, **62**, 2049; (c) Y. Sun, C. Qu, H. Chen, M. He, C. Tang, K. Shou, S. Hong, M. Yang, Y. Jiang, B. Ding, Y. Xiao, L. Xing, X. Hong and Z. Cheng, *Chem. Sci.*, 2016, **7**, 6203; (d) Y. Sun, X. Zeng, Y. Xiao, C. Liu, H. Zhu, H. Zhou, Z. Chen, F. Xu, J. Wang, M. Zhu, J. Wu, M. Tian, H. Zhang, Z. Deng, Z. Cheng and X. Hong, *Chem.*

Sci., 2018, **9**, 2092; (*e*) H. Zhou, S. Li, X. Zeng, M. Zhang, L. Tang, Q. Li, D. Chen, X. Meng and X. Hong, *Chin. Chem. Lett.*, 2020, **31**, 1382.

9 H. Wan, J. Yue, S. Zhu, T. Uno, X. Zhang, Q. Yang, K. Yu, G. Hong, J. Wang, L. Li, Z. Ma, H. Gao, Y. Zhong, J. Su, A. L. Antaris, Y. Xia, J. Luo, Y. Liang and H. Dai, *Nat. Commun.*, 2018, **9**, 1171.

10 J. Luo, Z. Xie, J. W. Lam, L. Cheng, H. Chen, C. Qiu, H. S. Kwok, X. Zhan, Y. Liu, D. Zhu and B. Z. Tang, *Chem. Commun.*, 2001, 1740.

11 (*a*) N. Alifu, A. Zebibula, J. Qi, H. Zhang, C. Sun, X. Yu, D. Xue, J. W. Y. Lam, G. Li, J. Qian and B. Z. Tang, *ACS Nano*, 2018, **12**, 11282; (*b*) D. Wang, M. M. S. Lee, G. Shan, R. T. K. Kwok, J. W. Y. Lam, H. Su, Y. Cai and B. Z. Tang, *Adv. Mater.*, 2018, **30**, 1802105; (*c*) S. Wang, J. Liu, C. C. Goh, L. G. Ng and B. Liu, *Adv. Mater.*, 2019, **31**, 1904447; (*d*) L. Zong, H. Zhang, Y. Li, Y. Gong, D. Li, J. Wang, Z. Wang, Y. Xie, M. Han, Q. Peng, X. Li, J. Dong, J. Qian, Q. Li and Z. Li, *ACS Nano*, 2018, **12**, 9532; (*e*) J. Dai, Y. Li, Z. Long, R. Jiang, Z. Zhuang, Z. Wang, Z. Zhao, X. Lou, F. Xia and B. Z. Tang, *ACS Nano*, 2020, **14**, 854; (*f*) G. Niu, X. Zheng, Z. Zhao, H. Zhang, J. Wang, X. He, Y. Chen, X. Shi, C. Ma, R. T. K. Kwok, J. W. Y. Lam, H. H. Y. Sung, I. D. Williams, K. S. Wong, P. Wang and B. Z. Tang, *J. Am. Chem. Soc.*, 2019, **141**, 15111; (*g*) J. Wang, X. Gu, P. Zhang, X. Huang, X. Zheng, M. Chen, H. Feng, R. T. K. Kwok, J. W. Y. Lam and B. Z. Tang, *J. Am. Chem. Soc.*, 2017, **139**, 16974; (*h*) D. Dang, Z. Qiu, T. Han, Y. Liu, M. Chen, R. T. K. Kwok, J. W. Y. Lam and B. Z. Tang, *Adv. Funct. Mater.*, 2018, **28**, 1707210; (*i*) D. Dang, H. Liu, J. Wang, M. Chen, Y. Liu, H. H. Y. Sung, I. D. Williams, R. T. K. Kwok, J. W. Y. Lam and B. Z. Tang, *Chem. Mater.*, 2018, **30**, 7892; (*j*) S. Liu, C. Chen, Y. Li, H. Zhang, J. Liu, R. Wang, S. T. H. Wong, J. W. Y. Lam, D. Ding and B. Z. Tang, *Adv. Funct. Mater.*, 2019, **30**, 1908125; (*k*) W. Qin, N. Alifu, J. W. Y. Lam, Y. Cui, H. Su, G. Liang, J. Qian and B. Z. Tang, *Adv. Mater.*, 2020, **32**, 2000364.

12 (*a*) D. Dang, H. Zhang, Y. Xu, R. Xu, Z. Wang, R. T. K. Kwok, J. W. Y. Lam, L. Zhang, L. Meng and B. Z. Tang, *ACS Nano*, 2019, **13**, 11863; (*b*) D. Li, W. Qin, B. Xu, J. Qian and B. Z. Tang, *Adv. Mater.*, 2017, **29**, 1703643; (*c*) G. Niu, R. Zhang, J. P. C. Kwong, J. W. Y. Lam, C. Chen, J. Wang, Y. Chen, X. Feng, R. T. K. Kwok, H. H. Y. Sung, I. D. Williams, M. R. J. Elsegood, J. Qu, C. Ma, K. S. Wong, X. Yu and B. Z. Tang, *Chem. Mater.*, 2018, **30**, 4778; (*d*) J. Liu, C. Chen, S. Ji, Q. Liu, D. Ding, D. Zhao and B. Liu, *Chem. Sci.*, 2017, **8**, 2782; (*e*) G. Niu, R. Zhang, Y. Gu, J. Wang, C. Ma, R. T. K. Kwok, J. W. Y. Lam, H. H. Sung, I. D. Williams, K. S. Wong, X. Yu and B. Z. Tang, *Biomaterials*, 2019, **208**, 72; (*f*) W. Qin, K. Li, G. Feng, M. Li, Z. Yang, B. Liu and B. Z. Tang, *Adv. Funct. Mater.*, 2014, **24**, 635.

13 J. Qi, C. Sun, A. Zebibula, H. Zhang, R. T. K. Kwok, X. Zhao, W. Xi, J. W. Y. Lam, J. Qian and B. Z. Tang, *Adv. Mater.*, 2018, **30**, 1706856.

14 J. Lin, X. Zeng, Y. Xiao, L. Tang, J. Nong, Y. Liu, H. Zhou, B. Ding, F. Xu, H. Tong, Z. Deng and X. Hong, *Chem. Sci.*, 2019, **10**, 1219.

15 Y. Li, Y. Liu, Q. Li, X. Zeng, T. Tian, W. Zhou, Y. Cui, X. Wang, X. Cheng, Q. Ding, X. Wang, J. Wu, H. Deng, Y. Li, X. Meng, Z. Deng, X. Hong and Y. Xiao, *Chem. Sci.*, 2020, **11**, 2621.

16 Q. Li, Q. Ding, Y. Li, X. Zeng, Y. Liu, S. Lu, H. Zhou, X. Wang, J. Wu, X. Meng, Z. Deng and Y. Xiao, *Chem. Commun.*, 2020, **56**, 3289.

17 (*a*) Q. Fu, R. Zhu, J. Song, H. Yang and X. Chen, *Adv. Mater.*, 2019, **31**, 1805875; (*b*) C. Liu, S. Zhang, J. Li, J. Wei, K. Mullen and M. Yin, *Angew. Chem., Int. Ed.*, 2019, **58**, 1638; (*c*) K. Pu, J. Mei, J. V. Jokerst, G. Hong, A. L. Antaris, N. Chattopadhyay, A. J. Shuhendler, T. Kurosawa, Y. Zhou, S. S. Gambhir, Z. Bao and J. Rao, *Adv. Mater.*, 2015, **27**, 5184; (*d*) Y. Liu, S. Wang, Y. Ma, J. Lin, H. Y. Wang, Y. Gu, X. Chen and P. Huang, *Adv. Mater.*, 2017, **29**, 1606129.

18 Z. Sheng, B. Guo, D. Hu, S. Xu, W. Wu, W. H. Liew, K. Yao, J. Jiang, C. Liu, H. Zheng and B. Liu, *Adv. Mater.*, 2018, **30**, 1800766.

19 D. Dang, D. Yu and E. Wang, *Adv. Mater.*, 2019, **31**, 1807019.

20 R. Hu, E. Lager, A. A. Aguilar, J. Liu, J. W. Y. Lam, H. H. Y. Sung, I. D. Williams, Y. C. Zhong, K. Wong, E. P. Cabrera and B. Z. Tang, *J. Phys. Chem. C*, 2009, **113**, 15845.

21 J. Mei, N. L. C. Leung, R. T. K. Kwok, J. W. Y. Lam and B. Z. Tang, *Chem. Rev.*, 2015, **115**, 11718.

22 X. Zheng, Q. Peng, L. Zhu, Y. Xie, X. Huang and Z. Shuai, *Nanoscale*, 2016, **8**, 15173.

23 H. Nie, K. Hu, Y. Cai, Q. Peng, Z. Zhao, R. Hu, J. Chen, S. J. Su, A. Qin and B. Z. Tang, *Mater. Chem. Front.*, 2017, **1**, 1125.

24 (*a*) K. Li and B. Liu, *J. Mater. Chem.*, 2012, **22**, 1257; (*b*) W. Qin, D. Ding, J. Liu, W. Z. Yuan, Y. Hu, B. Liu and B. Z. Tang, *Adv. Funct. Mater.*, 2012, **22**, 771.

25 Y. Xu, H. Zhang, N. Zhang, X. Wang, D. Dang, X. Jing, D. Xi, Y. Hao, B. Z. Tang and L. Meng, *ACS Appl. Mater. Interfaces*, 2020, **12**, 6814.

26 (*a*) W. Wu, Y. Yang, Y. Yang, Y. Yang, K. Zhang, L. Guo, H. Ge, X. Chen, J. Liu and H. Feng, *Small*, 2019, **15**, 1805549; (*b*) Y. Li, Z. Cai, S. Liu, H. Zhang, S. T. H. Wong, J. W. Y. Lam, R. T. K. Kwok, J. Qian and B. Z. Tang, *Nat. Commun.*, 2020, **11**, 1255.

27 Z. Tao, G. Hong, C. Shinji, C. Chen, S. Diao, A. L. Antaris, B. Zhang, Y. Zou and H. Dai, *Angew. Chem., Int. Ed.*, 2013, **52**, 13002.

28 T. Liu, L. Zhu, C. Zhong, G. Xie, S. Gong, J. Fang, D. Ma and C. Yang, *Adv. Funct. Mater.*, 2017, **27**, 1606384.

29 M. Mone, S. Tang, P. Murto, B. A. Abdulahi, C. Larsen, J. Wang, W. Mammo, L. Edman and E. Wang, *Chem. Mater.*, 2019, **31**, 9721.

30 D. Wang, M. M. S. Lee, W. Xu, G. Shan, X. Zheng, R. T. K. Kwok, J. W. Y. Lam, X. Hu and B. Z. Tang, *Angew. Chem., Int. Ed.*, 2019, **58**, 5628.

31 C. Li, Y. Zhang, M. Wang, Y. Zhang, G. Chen, L. Li, D. Wu and Q. Wang, *Biomaterials*, 2014, **35**, 393.

32 A. K. Iyer, G. Khaled, J. Fang and H. Maeda, *Drug Discovery Today*, 2006, **11**, 812.